Heliyon 11 (2025) e41720

Contents lists available at ScienceDirect

Heliyon

journal homepage: www.cell.com/heliyon

Research article

Development of functionalized biochar composites for enhanced boron adsorption from aqueous solutions

Sanaz Amirshekari [a], Saeid Shafiei [a], Mahboobeh Zahedifar [b,*], Hossein Shekofteh [a]

[a] Department of Soil Science, Faculty of Agriculture, University of Jiroft, Jiroft, 7867161167, Iran
[b] Department of Chemistry, Faculty of Science, University of Jiroft, Jiroft, 7867161167, Iran

ARTICLE INFO

Keywords:
Lignocellulosic biomass
Wastewater treatment
Adsorption

ABSTRACT

This study focuses on developing biochar-based adsorbents with high adsorption capacity and rapid adsorption rates for removing boron from aqueous solutions. Hydroxy-enriched biochar composites (BC (carboxylated biochar), BC-PDA (polydopamine loaded biochar), MBC-PDA (polydopamine loaded magnetic biochar), BC-AlOOH (AlOOH loaded biochar), and BC-$ZnCl_2$ (biochar modified by $ZnCl_2$)) were synthesized specifically for boron adsorption to utilize the superior adsorption capacity of biochar. All adsorbents were synthesized using straightforward experimental techniques from date palm cellulosic fibers as promising lignocellulose feedstock and subjected to various characterization methods. Boron adsorption kinetics, isotherms, mechanism, and adsorbent recycling were investigated using batch adsorption experiments. The experimental results showed adsorption capacity values of 14, 20.5, 21.5, 43.2, and 44.2 mg/g for BC, BC-PDA, MBC-PDA, BC-AlOOH, and BC-$ZnCl_2$ composites at 360 min. The prominent adsorption capacity of the synthesized adsorbents was related to the abundant existence of -OH functional groups on the BC adsorbent surface and the abundance of pores widely distributed throughout the surface, facilitating the chemical and physical adsorption of boron. The synthesized adsorbents exhibited a promoted boron adsorption capacity and ease of recovery and reusability.

1. Introduction

While boron is essential for plant and animal health, it can cause environmental and health issues when excessed [1]. Continuous low-level absorption of boron compounds can pose health risks, especially in areas with high concentrations in water supplies [2]. The increasing concentration of boron in the environment can be attributed to various factors such as desalination or water-rock interaction and degassing of magma intrusive in thermal waters [3,4], which may pose a severe toxicity threat to plants and animals [5] resulting in irreversible ecosystem damage [1,6]. Therefore, removing it from aqueous solutions, seawater, and saline water is crucial. A range of technologies have been developed for boron removals, such as forward osmosis [7] and membrane distillation [8], electrocoagulation [9], chemical precipitation [10], ion exchange [11], and adsorption [12].

Adsorption, in particular, has been highlighted as an essential method with various sorbents, including activated carbon [13,14], chelating resins [15], and industrial waste materials for boron removal [16]. Essentially, the adsorption method lies in the intermolecular attractive forces between the solution and the solid surface, along with choosing the proper adsorbent [17]. Recently,

* Corresponding author.
E-mail address: mzahedi@ujiroft.ac.ir (M. Zahedifar).

https://doi.org/10.1016/j.heliyon.2025.e41720
Received 26 September 2024; Received in revised form 19 December 2024; Accepted 3 January 2025
Available online 9 January 2025

biosorbents have become increasingly desirable due to their environmental benefits and adsorption potential [18,19].

Biochar, a biosorbent produced by biomass pyrolysis, has been extensively studied as an adsorbent for removing contaminants from water [20,21]. Biochar benefits from different characteristics as an adsorbent: high specific surface area, porous nature, widespread availability, and affordability [22,23]. Feedstocks and pyrolysis conditions can affect the biochar adsorption capacity. During pyrolysis, the biochar matrix experiences structural transformations, increasing in aromaticity and structural order as the temperature rises. The sp2-hybridized carbon matrix's defects and oxygen-containing functional groups are responsible for the biochar activity [24–26]. Biochar synthesis can be accomplished using lignocellulosic biomass, which is mainly constituents of cellulose, hemicellulose, and lignin. Date palm fibers are a promising source of lignocellulosic materials. These fibers, obtained from the date palm tree trunks, have a high cellulosic content that makes them ideal as feedstock [27].

It has also been shown that biochar's adsorption capacity can significantly increase when its surface is functionalized. Several studies demonstrate that increased electrostatic effects significantly enhance hydroxy-functionalized biochar's adsorption capacity [28]. Hydroxyl groups on the biochar surface increased the electrostatic effect, leading to stronger adsorption capacity. Wan et al., reported a higher adsorption capacity of biochar when surface functionalization with hydroxy groups was applied, which is attributed to the increase in oxygen-containing functional groups on the biochar surface that enhanced adsorption capacity [29]. Zhao et al., further supported these findings, showing that biochar's adsorption capacity for tetracycline antibiotics was significantly improved after hydroxy functionalization [30]. These studies collectively suggest that hydroxy-functionalized biochar has a higher adsorption capacity, making it a promising material for various environmental applications.

Continuing our efforts to remove organic pollution by biosorbents [21,31,32], in this study, modified biochar composites were synthesized by straightforward experimental techniques for boron adsorption from aquas media. This work introduces a unique approach to developing hydroxy-enriched biochar composites synthesized from date palm cellulosic fibers, representing an innovative and sustainable approach for boron adsorption from aqueous media. Unlike conventional adsorbents, the hydroxy-enriched biochar composites demonstrate superior adsorption performance due to their enhanced electrostatic interactions and increased oxygen-containing functional groups. This study uniquely combines lignocellulosic biomass from date palm fibers, a cost-effective and renewable feedstock, with straightforward functionalization techniques to create adsorbents with high efficiency, recyclability, and tailored morphology. The outcomes offer a promising, environmentally friendly solution to address the pressing issue of boron contamination in water.

2. Material and methods

The date palm fiber biomass was gathered from university of Jiroft date garden, Jiroft, Iran. Merck and Sigma-Aldrich were the sources of chemicals, reagents, and solvents that were used in this work. The prepared BC adsorbents were analyzed for their crystalline structure using XRD patterns by X'PertPro diffractometer (Panalytical, Almelo, The Netherlands, Cu Ka radiation, wavelength = 1.54 Å). A Bruker Tensor 27 Fourier transform infrared spectrometer was used to collect FT-IR spectra using a KBr pellet. The size and structure of BC adsorbents were analyzed using transmission electron microscopy (TEM; EM10c-100 kV) and scanning electron microscopy (SEM; SIGMA VP from Carl Zeiss Inc., Jena, Germany) techniques. Energy-dispersive X-ray spectroscopy (EDS) was also performed to gather relevant data. TGA (STA503, Germany) was utilized to test the prepared photocatalyst's thermal stability. The boron adsorption wavelength was recorded using a PerkinElmer, USA Lambda 25 double-beam spectrophotometer.

2.1. Synthesis of raw biochar

The date palm fiber biomass was washed, dried in an oven at 60 °C, ground, sieved, and then pyrolyzed without oxygen flow at 450 °C for 2 h to produce raw biochar [21].

2.2. Synthesis of biochar functionalized carboxylic acid (BC)

A reaction mixture containing 3 g of raw biochar and 100 mL of HNO_3 was conducted at 60 °C for 12 h. The reaction mixture was supplemented by adding 100 mL of deionized water, after which the resulting black precipitate was separated through centrifugation at 5000 rpm for 10 min. Drying of carboxylated biochar (BC) was carried out for 12 h at 50 °C [33].

2.3. Synthesis of BC-PDA

Polydopamine-coated BC (BC-PDA) was synthesized using the following method. A mixture of 0.4 g dopamine hydrochloride in Tris-HCl (220 mL, 10 mM, pH = 8.5) was stirred for 15 min. Then, 0.4 g of BC was added to the mixture and stirred at ambient temperature for 24 h. After 10 min centrifuge at 5000 rpm, the residue was washed with a solution of water/ethanol (50:50) three times and then dried at 60 °C to obtain BC-PDA [34].

2.4. Synthesis of MBC-PDA

1.0 g of BC-PDA, 2.7 g $FeCl_3.6H_2O$, and 1 g $FeCl_2.4H_2O$ were added to 50 mL deionized water under nitrogen flow. After 5 min, under vigorous stirring 11 mL of NH_3 25 % was added dropwise for 1 h to produce black powder of MBC-PDA. Then, a magnet was used to collect the black solid, followed by three times rinsing with distilled water and drying for 6 h at 60 °C [35].

2.5. Synthesis of BC-AlOOH composite

First, 2g of date palm cellulosic fibers feedstock was added to an aluminum chloride solution (10 g of $AlCl_3.6H_2O$ in 15 mL distilled water) and then stirred for 2 h. Afterward, the mixture was dried in an oven for 24 h at 70 °C and then pyrolyzed for 1 h at 600 °C while preventing oxygen flow. BC-AlOOH was obtained by washing the product three times with distilled water and then drying at 60 °C [36].

2.6. Synthesis of BC-$ZnCl_2$

First, 2g of date palm cellulosic fibers feedstock was added to a solution containing 10g of $ZnCl_2$ in 15 mL of distilled water. The mixture was then stirred for 2 h. The next step involved dehydrating the mixture at 70 °C for 24 h. The residue was pyrolyzed for 1 h at 600 °C while preventing oxygen flow. BC- $ZnCl_2$ was obtained by washing the product three times with distilled water and then drying at 60 °C [37].

2.7. Boron adsorption

The adsorption capacity of adsorbents against boric acid in water was tested using batch adsorption experiments. The pH of the samples was regulated during the experiments by using solutions of 0.1 M HCl or 0.1 M NaOH. To determine the adsorption capacity of adsorbents, different concentrations of boric acid solution (10, 30, 50, 70, 90, and 110 ppm) were added to the given amount of composites. After 6 h of vigorous stirring, the adsorbent was separated from the solution via centrifugation at 4000 rpm for 10 min upon reaching equilibrium. The azomethine-H spectrophotometric method was employed to determine the boron concentration at $\lambda =$ 420 nm [38].

The sorbents' adsorption efficiency (q) was calculated using Eq (1).

$$q = \frac{(C_0 - C_t) \times V}{m} \tag{1}$$

Where q is the asdsorption capacity (mg/g), V represents the solution volume (L), and m (g) is the sorbent weight.

2.7.1. Boron adsorption kinetic

A 50 mg/L boron concentration was used as initial concentration of boric acid for the adsorption kinetics experiments. The adsorbent concentration were 100 mg/50 mL (BC, BC-PDA, and MBC-PDA) and 50 mg/50 mL (BC-AlOOH and BC-$ZnCl_2$). Kinetic experiments were conducted at pH 8 (BC-PDA and MBC-PDA) and pH 9 (BC, BC-AlOOH, and BC-$ZnCl_2$). Samples were collected for boron analysis after reaction times of 20, 40, 60, 80, 100, 120, 140, 160, 180, 200, 220, 240, 260, 280, 300, 320, 340, and 360 min. The process of adsorption kinetics can be evaluated by using two kinetic models - pseudo-first-order and pseudo-second-order. (Eqs. (2) and (3)).

$$q_t = q_e \left(1 - e^{k_1 t}\right) \tag{2}$$

$$q_t = \frac{q_e^2 \, k_2 \, t}{1 + q_t \, k_2 \, t} \tag{3}$$

Equilibrium adsorption capacity is represented by q_e (mg/g), while the adsorption capacity at a given time is denoted as q_t (mg/g). The pseudo-first-order equilibrium rate constant, k_1 (1/min), and the pseudo-second-order equilibrium rate constant, k_2 (g/mg min), describe the adsorption kinetics.

The intraparticle diffusion model is employed to elucidate the diffusion mechanism by eq (4):

$$q_t = k_i \, t^{1/2} + C \tag{4}$$

In this eq, k_i represents the rate constant, C is a constant that varies for each experiment (measured in mg/g), and the adsorption capacity at a given time is denoted as q_t (mg/g). By plotting q_t against the t^(1/2) curves were obtained.

2.7.2. Boron adsorption isotherm

The adsorption of boron as a function of its initial concentration was performed at ambient temperature for 360 min. Adsorbent concentrations of 20, 40, 60, 80, 100, 120, 140, 160, 180, and 200 mg/50 mL were investigated for all adsorbents. Experiments were conducted across a pH range of 4–11 for all adsorbents.

Using the following equations (Eq. (5) and Eq. (6)), the Langmuir and Freundlich isotherm models were employed to fit the data:

$$q_e = \frac{q_m \, k_L \, C_e}{1 + k_L \, C_e} \tag{5}$$

$$q_e = k_F \, C_e^{1/n} \tag{6}$$

The maximum adsorption capacity of the adsorbent is denoted as q_m (mg/g), while q_e (mg/g) represents the equilibrium adsorption capacity of the biochar-based adsorbent for boron removal. C_e (mg/L) is used to indicate the concentration of boron after equilibrium adsorption on the adsorbent. K_L is the Langmuir constant, and K_F is the Freundlich constant for the adsorption capacity. Lastly, the Freundlich constant for the adsorption strength is represented by 1/n.

2.8. Recyclability of adsorbents

Three rounds of adsorption-desorption tests were conducted to evaluate the reusability of the synthesized adsorbents. The adsorption tests were accomplished at ambient temperature for 6 h to determine the boron concentration and calculate the adsorption capacity (q_e). The collected adsorbents were immersed in HCl (20 mL, 0.1 M) for 48 h and then rinsed with deionized water to neutralize and dried for subsequent regeneration experiments.

3. Results and discussion

A series of hydroxy-functionalized biochar-based adsorbents were synthesized from palm date waste as biomass using straightforward methods (Fig. 1). Biochar functionalized carboxylic acid (BC) was produced by reacting raw biochar with nitric acid, which increased the oxygen functional groups, such as carboxylic acid and hydroxy groups. To produce BC-PDA, dopamine hydrochloride was polymerized on the surface of the raw biochar, which already contains many hydroxy functional groups. MBC-PDA was synthesized by magnetizing BC-PDA with Fe_3O_4 NPs to facilitate separation from aqueous media. BC-AlOOH was produced using a simple method through the pyrolysis of a mixture of aluminum chloride ($AlCl_3$) and palm date waste biomass at 600 °C, resulting in an adsorbent with numerous hydroxy functional groups on its surface. Finally, BC-$ZnCl_2$ was prepared using a straightforward approach by pyrolyzing a mixture of zinc chloride ($ZnCl_2$) and palm date waste biomass at 600 °C, which also featured hydroxy functional groups on its surface.

The prepared adsorbents were characterized by different characterization methods.

3.1. TEM

Fig. 2 shows TEM micrographs of BC, BC-PDA, BC-AlOOH, and BC-$ZnCl_2$ compounds. The TEM image of BC (Fig. 2a) shows amorphous and coarse granular monoliths. In the TEM image of BC-PDA, by polymerizing dopamine on the BC surface (Fig. 2b), PDA created uniform coating spheres on the BC surface by interacting strongly with BC functional groups. The organic sphere has a uniform size between 150 and 200 nm, as seen in TEM images. TEM image of the BC-AlOOH composite revealed surface wrinkles that may promote chemical deposition by increasing nanoparticle surface area. (Fig. 2c). According to the TEM image of BC- $ZnCl_2$, there are spherical particles consisting of Zn_2SiO_4 and SiO_2 (Fig. 2d).

3.2. SEM-EDS

The morphology and elemental composition of BC, BC-PDA, MBC-PDA, BC-AlOOH, and BC- $ZnCl_2$ samples were analyzed by SEM-EDS. In Fig. 3a, the BC matrix appeared as a carbon skeleton with a relatively porous structure and smooth surface morphology. The SEM image of BC-PDA (Fig. 3b) depicted a rough surface with numerous closely connected microspheres on the BC surface, indicating the successful polymerization of dopamine with sphere shapes on the BC surface. The PDA sphere size is approximately 200 nm. After magnetization, surface roughness of MBC-PDA was increased, and Fe_3O_4 nanoparticles with an average size of 35 nm were developed on the surface and channels of BC-PDA (Fig. 3c and d).

The BC-AlOOH nanocomposite morphological structure is shown in Fig. 3e. Compared with BC, BC-AlOOH contained an abundance of pores widely distributed throughout the surface following pyrolysis. (Fig. 3e). It had been observed that AlOOH flakes grew with a homogenous and dense pattern throughout BC. Fig. 3f shows the SEM image of synthesized BC-$ZnCl_2$. Compared to BC with a smooth surface morphology, BC-$ZnCl_2$ exhibits numerous dense and evenly distributed pores across its surface as pyrolyzed. BC-$ZnCl_2$'s morphology is created by the combustion gas emitted during high-temperature pyrolysis.

EDS analysis was conducted to examine the elemental composition of BC, BC-PDA, MBC-PDA, BC-AlOOH, and BC- $ZnCl_2$ composites. EDS analysis of BC revealed the presence of C, O, and Si elements (Fig. 4a). Biochar samples often contain silicon impurities. In the EDS analysis of BC-PDA, C, O, and N elements were detected (Fig. 4b), suggesting successful preparation of polydopamine

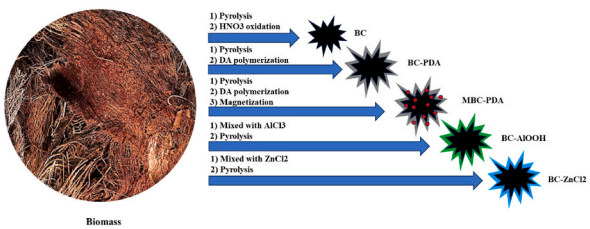

Fig. 1. Synthesis way of BC-adsorbents from lignocellulosic biomass of date palm.

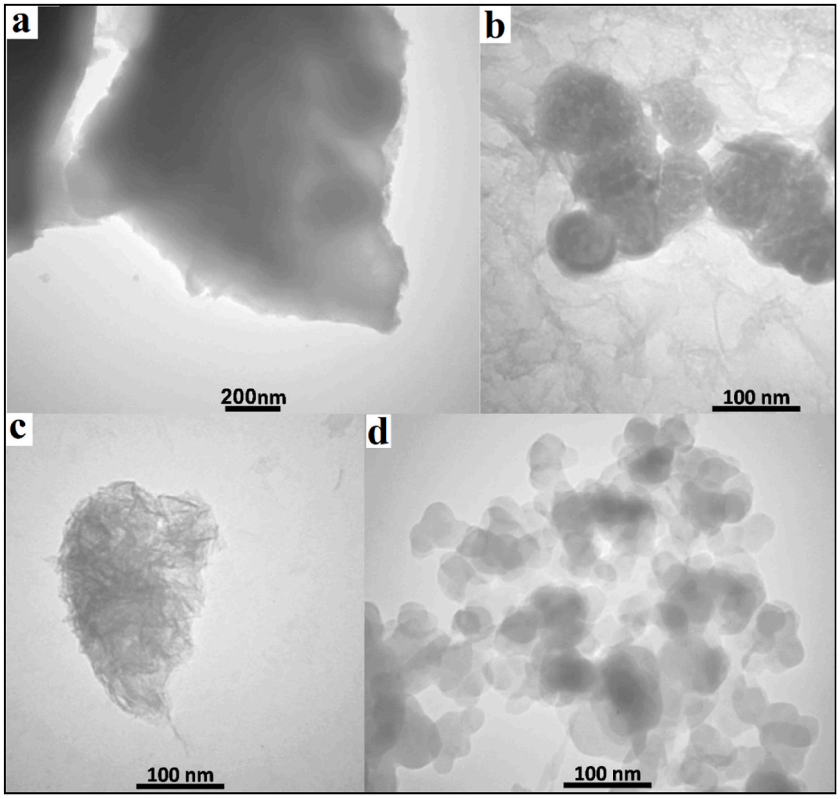

Fig. 2. TEM micrographs of a) BC, b) BC-PDA, c) BC-AlOOH, and d) BC-$ZnCl_2$.

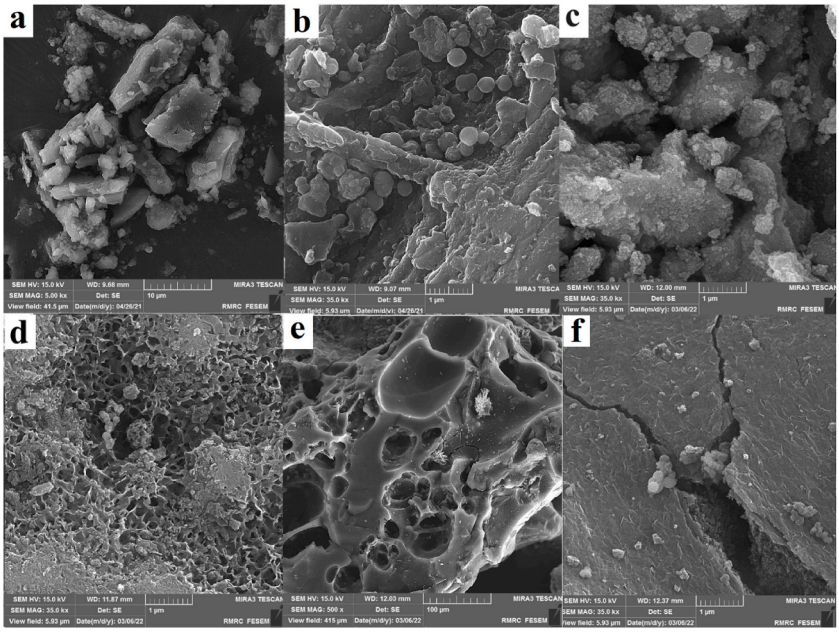

Fig. 3. FE-SEM images of a) BC, b) BC-PDA, c) MBC-PDA, d) BC-AlOOH, and e, f) BC-$ZnCl_2$ at different magnification.

functionalized biochar. EDS analysis of MBC-PDA revealed Fe, C, O, and N elements, which confirmed successful magnetization of BC-PDA (Fig. 4c). BC-AlOOH's EDS analysis confirmed that the nanoflakes on its surface were composed of aluminum and oxygen, which matched the chemistry of aluminum oxides (Fig. 4d). BC- $ZnCl_2$ EDS results indicated that Zn was successfully deposited on the BC

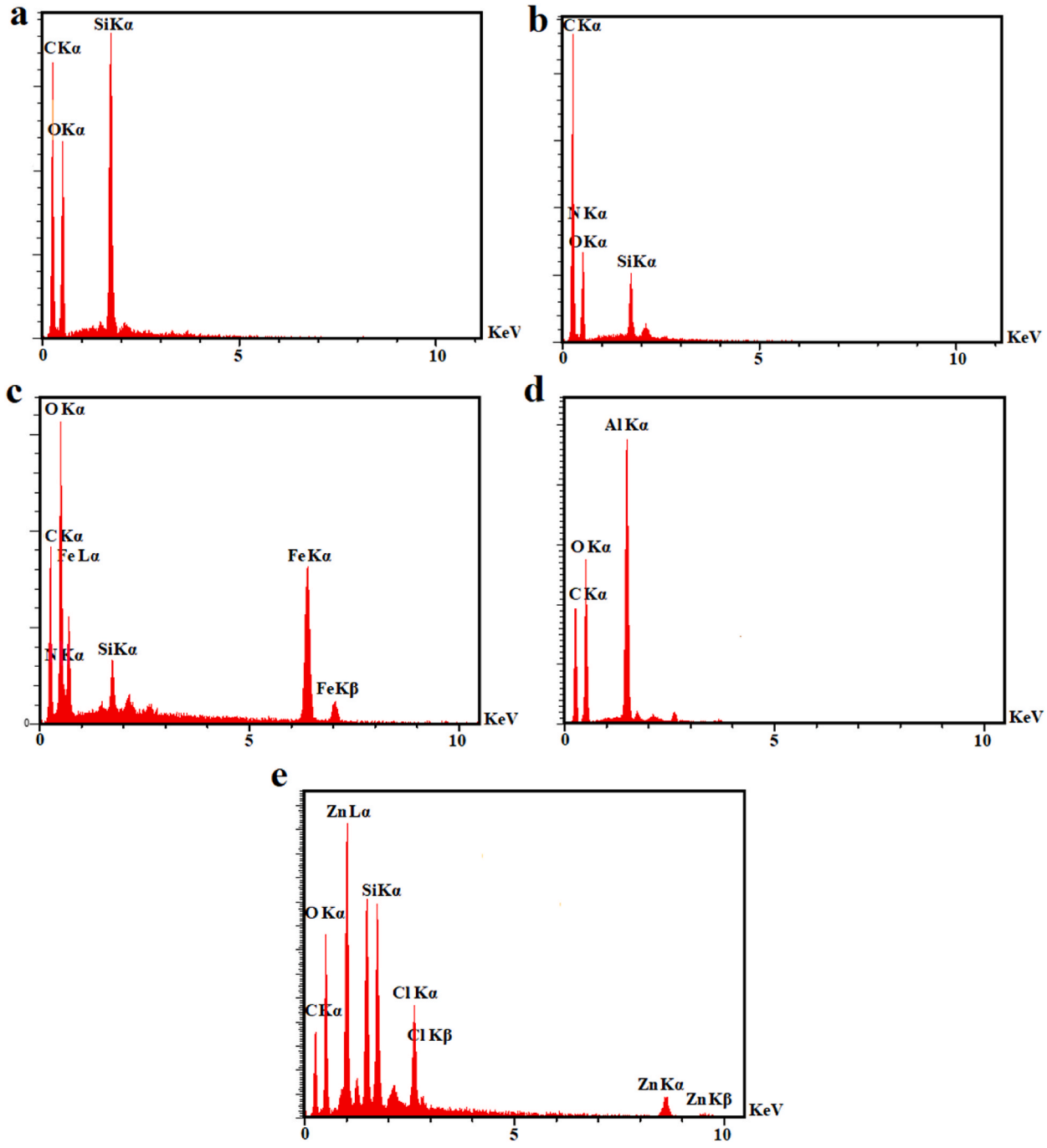

Fig. 4. EDS analysis of a) BC, b) BC-PDA, c) MBC-PDA, d) BC-AlOOH, and e) BC-$ZnCl_2$.

surface (Fig. 4e).

3.3. FT-IR

Fig. 5 displays the infrared spectra of raw biochar, BC, BC-PDA, MBC-PDA, BC-AlOOH, and BC-$ZnCl_2$ composites. The comparison of the FT-IR spectra of BC and raw biochar reveals some significant differences. Compared to raw biochar, the FT-IR spectrum of BC shows board peaks at 3600-3100 cm^{-1} and a sharp peak at 1720 cm^{-1}, suggesting that carboxylic acid groups have formed on the biochar surface after reaction with HNO_3 (Fig. 5a and b) [33]. Strong peaks around 1106 cm^{-1} are also attributed to the C-O-C bond stretching vibration (Fig. 5a and b) [33,39]. For BC-PDA, the bands observed at 1596 cm^{-1} and 1113 cm^{-1} can be related to the N-H

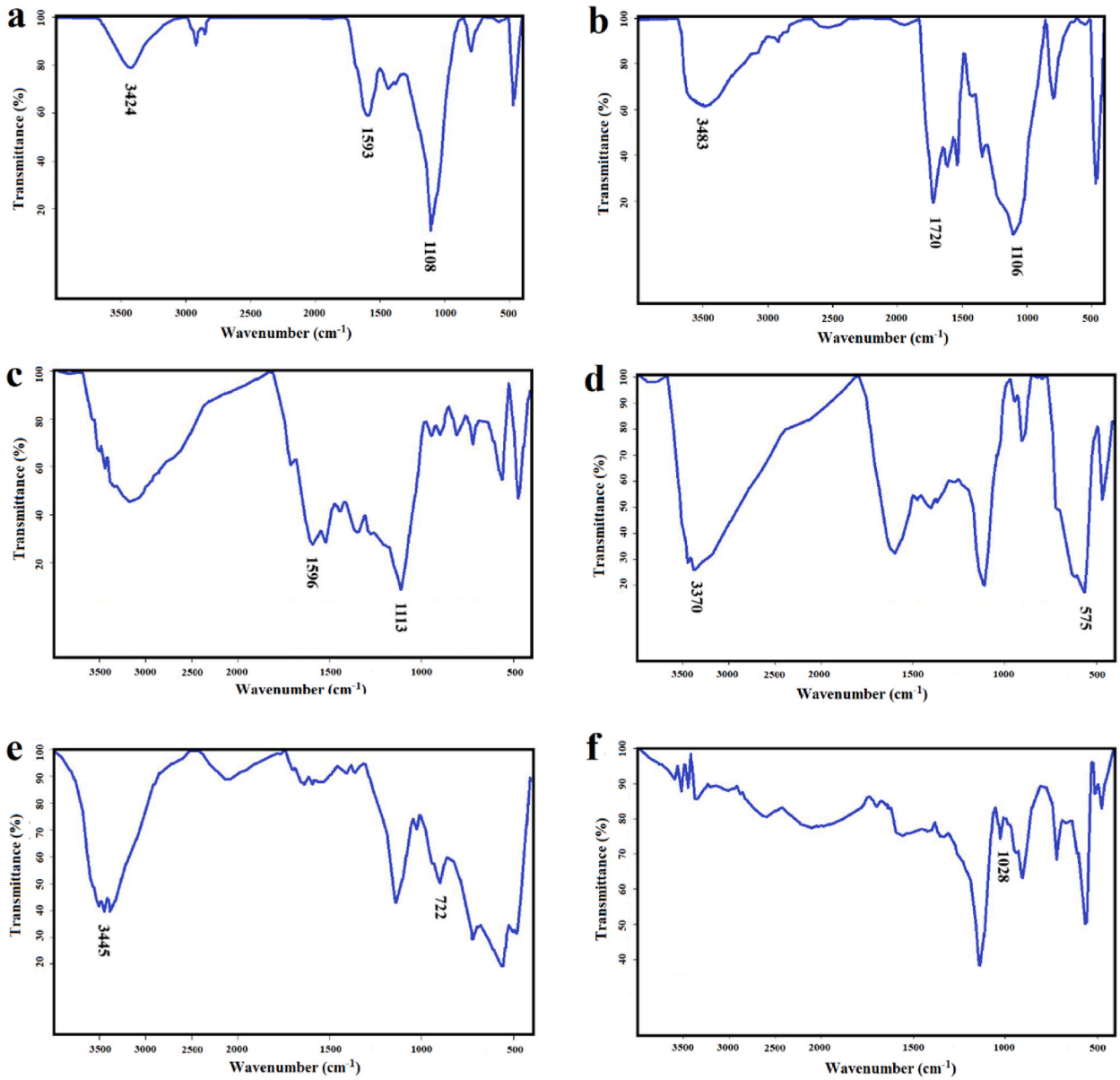

Fig. 5. FTIR spectra of a) raw biochar, b) BC, c) BC-PDA, d) MBC-PDA, e) BC-AlOOH, and f) BC-$ZnCl_2$ composites.

bending vibration and C-OH stretching vibration of dopamine groups, respectively, confirmed successful dopamine polymerization on the BC surface (Fig. 5c) [40]. According to the FT-IR spectra of MBC-PDA (Fig. 5d), there is a noticeable vibration at 575 cm^{-1}, which is associated with the Fe-O vibrational band of Fe_3O_4 NPs characteristic peak [35], indicating successful magnetization of BC-PDA. Furthermore, the board peaks at 3700-2500 cm^{-1} for both BC-PDA and MBC-PDA, corresponding to O-H stretching vibrations, confirming the hydroxy functionalization on the adsorbents surface.

BC-AlOOH (Fig. 5e) exhibited stronger stretching vibrations than raw biochar around 3400 cm^{-1} [41], which can be attributed to a greater abundance of hydroxy groups and a stronger hydrogen bonding network, a crucial property of the AlOOH layer. The Al-O bonds could be responsible for the peak at 722 cm^{-1} [42]. BC-$ZnCl_2$ (Fig. 5f) exhibits weak peaks of -OH stretching vibrations compared to raw biochar (Fig. 5a), which agrees with the report of Xia et al. The band at 1028 cm^{-1} is related to the hydroxy groups bending vibrations of Zn-OH [37].

3.4. TGA

Thermal stability of synthesized samples is determined by thermogravimetric analysis (TGA). All samples showed weight loss at

70–150 °C due to the evaporation of trapped water or solvent in BC composites (Fig. 6). BC begins to lose weight around 250–550 °C and releases H_2O, CO_2, and CO molecules due to the decomposition of the carbon skeleton during the combustion process [40]. The weight loss observed in the TGA curve of BC-PDA between 150 and 300 °C results from PDA degradation. On the other hand, MBC-PDA demonstrates higher thermal resistance than BC-PDA due to the strong thermal stability of Fe_3O_4 NPs. The prepared BC composites showed strong thermostability and minimal weight loss, as they did not decompose until high temperatures were reached. The remaining masses were 77.5 % for BC, 68.5 % for the BC-PDA, 78.1 % for the MBC-PDA, 73 % for the BC-AlOOH, and 91.7 % for the BC-ZnCl2.

3.5. XRD

The XRD patterns of BC-PDA, MBC-PDA, BC-AlOOH, and BC-$ZnCl_2$ composites are displayed in Fig. 7. In the XRD pattern of BC-PDA (Fig. 7a), a broad peak at 2θ = 23.9° indicates the existence of amorphous carbon in BC, comprising randomly oriented aromatic carbon sheets [34]. Amorphous carbon was produced through pyrolysis; a thermal decomposition process in which carbon is subjected to high temperatures in the absence of oxygen. As indicated by XRD results, the pyrolysis process fragments carbon atoms, which reassemble into random configurations of aromatic carbon sheets [43].

The MBC-PDA sample (Fig. 7b) showed reflection peaks at various angles, including 30.3° (1 1 1), 35.7° (2 2 0), 43.4° (3 1 1), 53.8° (4 2 2), 57.3° (5 1 1), 63.0° (4 4 0), and 74.6° (5 3 3), indicating the presence of cubic spinel ferrite structure for Fe_3O_4 nanoparticles (JCPDS PDF No. 01-075-0449) [44,45]. The XRD pattern of MBC-PDA reveals no pronounced BC peak, indicating the presence of turbostratic crystallites in the amorphous matrix (Fig. 7b) [33]. The sharp diffraction peaks in the XRD pattern of MBC-PDA indicate that Fe_3O_4 NPs were immobilized on BC-PDA surfaces with a high degree of crystallinity [46,47]. The high crystallinity explains the excellent magnetic properties of BC composites.

Fig. 7c shows the XRD pattern of BC-AlOOH. The diffraction peaks for AlOOH crystalline structure were observed at 13.8°, 28.3°, 38.3°, 49.0°, and 64.7°, corresponding to (020), (120), (031), (200), and (151) respectively [36]. The sharp XRD reflection peaks of BC-AlOOH (Fig. 7d) verify the high crystallization of the prepared particles. The BC-$ZnCl_2$ XRD pattern is presented in Fig. 7d. The X-ray diffraction analysis revealed that the peaks associated with quartz appeared at angles of 20.9° and 26.7° [38]. Peaks assigned to $Zn(OH)(NO_3)(H_2O)$ and $Zn_2(SiO_4)$ were found at 2θ (25.6°, 31.6°, 34.1°, 38.9°, 49.0°) and 2θ (22.1°, 27.9, 65.8°), respectively [37]. According to the XRD results, Zn on the biochar surface was mostly presented as Zn-OH.

3.6. Application of synthesized biochars for boron removal

3.6.1. Effect of pH

Fig. 8a shows the variation of boron adsorption capacity with pH to identify optimal adsorption pH. The adsorption capacity of all samples for boron increases as pH increases from 4 to 9. The adsorption capacity of BC, BC-AlOOH, and BC-$ZnCl_2$ was obtained at pH = 9 with q_e = 14, 43.2, and 44.2 mg/g, respectively. Meanwhile, for BC-PDA and MBC-PDA, the adsorption capacity was obtained at pH = 8 with q_e = 20.5 and 21.65 mg/g, respectively. A further increase in pH decreases boron adsorption capacity, as reported in various studies [48–50]. It has been shown that lower adsorption capacity is observed at acidic pH values, as depicted in Fig. 8a. As a result, at pH 8–9, boron is absorbed most efficiently, which is very close to boric acid's pKa (pH = 9.2).

Boric acid is present at pH values below 7, while borate ions are primarily found at pH values above 11. Increasing pH makes more borate ions available, resulting in more adsorption capacity. At weak alkaline pH values, boron adsorption is most effective due to the formation of stable boron complexes, instead of boric acid, on the adsorbent surface. As the pH level goes up, the uptake of boron decreases, which the existence of fewer types of boron complexes at higher pH levels can explain. Additionally, the borate ions start competing with the hydroxide ions in the solution for adsorption, which directly reduces the affinity of the adsorbent towards boron

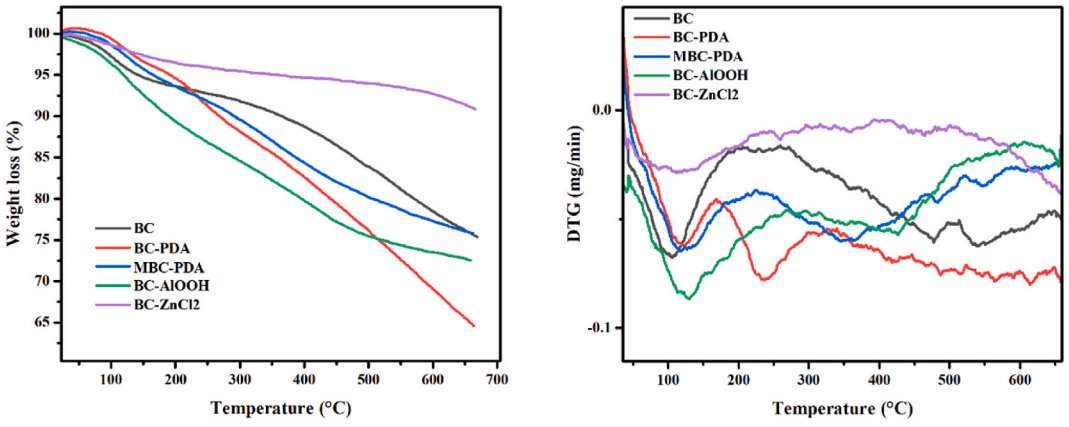

Fig. 6. The TGA analysis of BC, BC-PDA, MBC-PDA, BC-AlOOH, and BC-$ZnCl_2$.

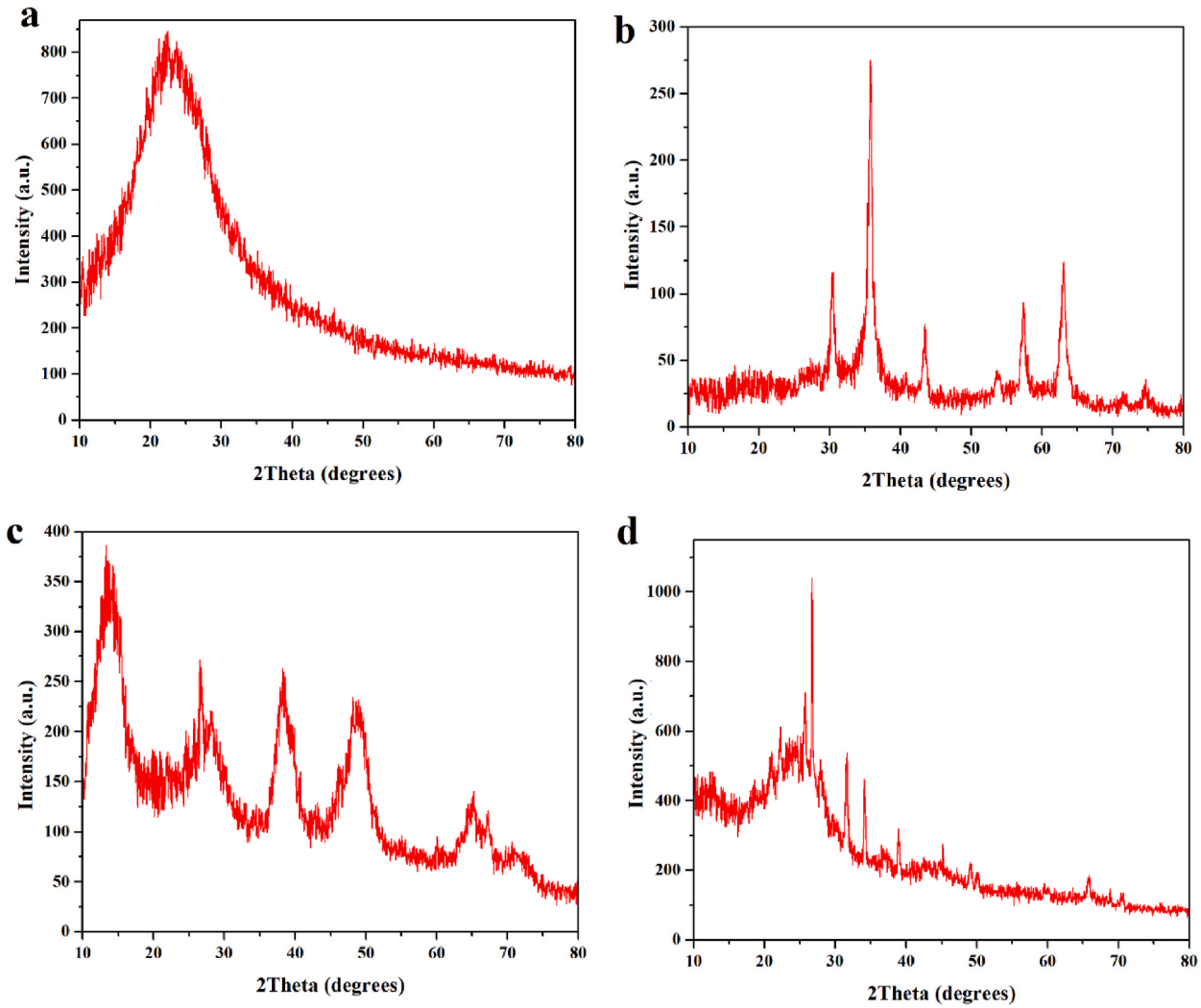

Fig. 7. The XRD patterns of BC-PDA, MBC-PDA, BC-AlOOH, and BC-$ZnCl_2$ composites.

ions [15,48].

3.6.2. *Effect adsorbent dosage*

Fig. 8b depicts the impact of the adsorbent amount on boron adsorption capacity. Various adsorbent dosages were tested, including 20, 50, 100, 150, and 200 mg/50 mL. As anticipated, boron adsorption capacity was increased by increasing the adsorbent dosage. A higher dosage of the adsorbent increases the number of adsorption sites, improving adsorption capacity [51,52]. However, the rate of boron removal does not increase linearly with dosage. The adsorption capacity does not significantly change with increasing adsorbent amounts. The adsorption capacity of BC-PDA and MBC-PDA adsorbents is obtained using a 100 mg/50 mL dosage while, for BC-AlOOH and BC-$ZnCl_2$ with a 50 mg/50 mL adsorbent dosage, the absorption capacity was achieved.

3.6.3. *Contact time effect*

Boron adsorption evaluation over time is depicted in Fig. 8c. All samples showed an increase in adsorption capacity up to 360 min of contact time. The equilibrium adsorption values of 14, 20.5, 21.5, 43.2, and 44.2 mg/g are obtained for BC-PDA, MBC-PDA, BC-AlOOH, and BC-$ZnCl_2$ composites after 220, 180, 160, 120, and 120 min, respectively. The adsorption capacity is initially increased due to the accessibility of available adsorption sites on the adsorbent surface as well as increased diffusion. Adsorbent surfaces are gradually saturated with time, releasing ions from their surfaces [53].

3.6.4. *Adsorption kinetics*

Under the optimum adsorption condition, the BC adsorbents demonstrate excellent adsorption performance, as shown in Fig. 8d. The adsorption rate gradually increases as the contact time prolongs, reaching equilibrium after 360 min. The high adsorption capacity

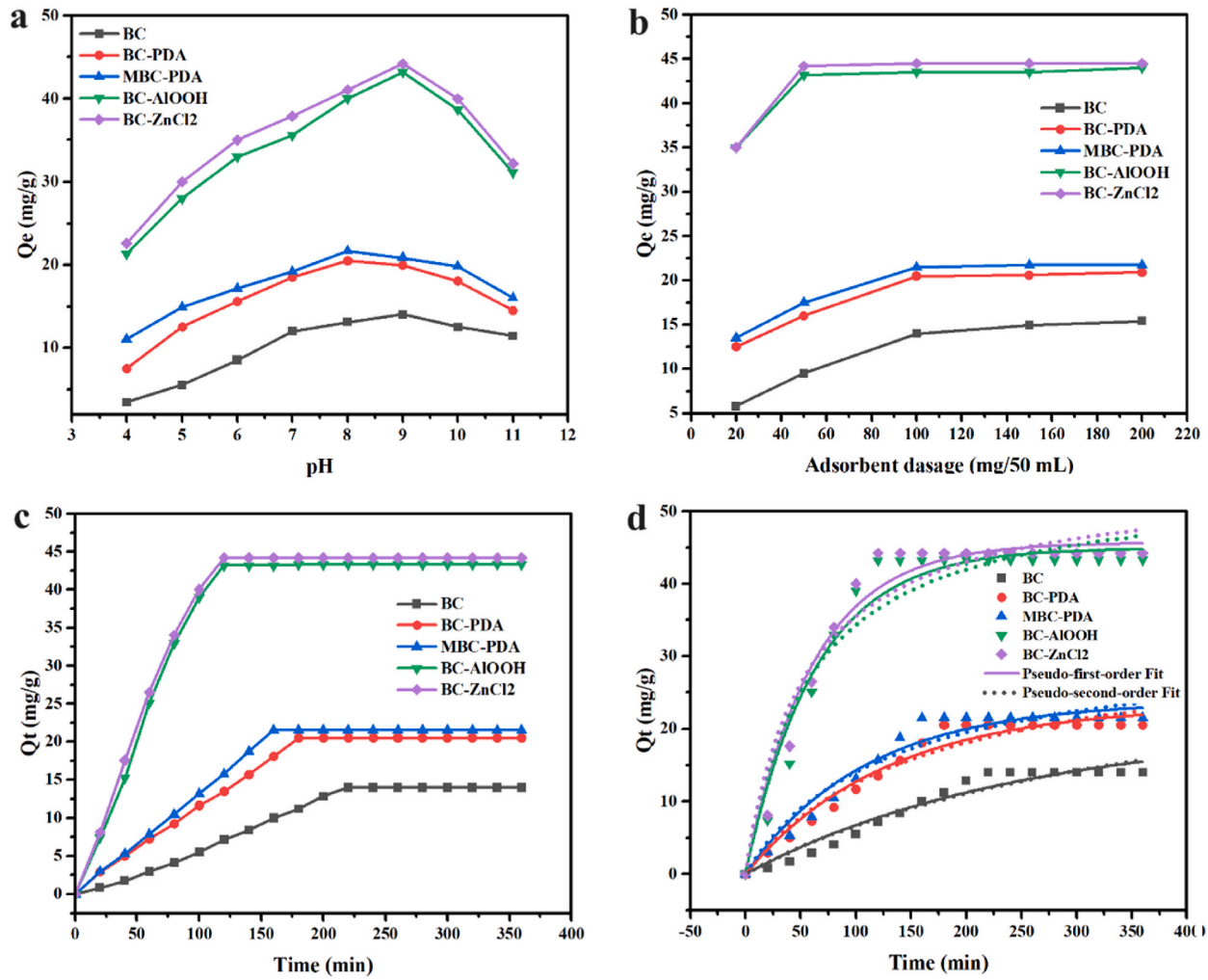

Fig. 8. a) pH effect b) adsorbent dosage effect, and c) time effect on the adsorption performance. d) The dynamical non-linear kinetic model.

of BC adsorbents, specifically BC-AlOOH and BC-$ZnCl_2$, is due to the abundance of hydroxy functional sites and the porous nature of BC. Pseudo-first-order and second-order kinetic models (Eqs. (2) and (3)) were applied to provide the adsorption kinetic data of BC adsorbents. Fig. 8d and Table 1 show the fitting curves and the related data. The pseudo-first-order kinetic model correlates better with the kinetic curves than the pseudo-second-order kinetic model, based on the correlation coefficients R^2 obtained from the linear fit. For all adsorbents, the calculated q_e by the pseudo-first-order model was closer to that obtained experimentally. These results suggest that the adsorption mechanism can be more accurately explained by the pseudo-first-order kinetic model. All adsorption steps are combined in the pseudo-first-order model, including external diffusion, internal diffusion, and adsorption [54].

Table 1
Adsorption kinetic data by pseudo-first-order and second-order models.

Model	Pseudo-second-order model				
Adsorbent	BC	BC-PDA	MBC-PDA	BC-AlOOH	BC-$ZnCl_2$
q_e	32.61052	32.19634	31.9006	54.14831	54.54293
k_2	7.91202E-5	1.9977E-4	2.47075E-4	3.18955E-4	3.41419E-4
R^2	0.94876	0.95307	0.9399	0.92803	0.9347
Model	Pseudo-First-order model				
q_e	20.05034	23.23728	23.72888	44.92025	45.68127
k_1	0.0041	0.00792	0.00919	0.01572	0.01647
R^2	0.95376	0.9663	0.95824	0.96321	0.96972

3.6.5. Adsorption isotherms

Adsorption equilibrium constants and maximum adsorption capacities are calculated using isothermal adsorption tests to further investigate the adsorption behavior of the adsorbent. The effect of varying initial concentrations of boric acid on the adsorption behavior of BC adsorbents (BC-PDA, MBC-PDA, BC-AlOOH, and BC-$ZnCl_2$) was examined through isothermal adsorption experiments. Table 2 and Fig. 9 summarize the Langmuir and Freundlich models' data and the corresponding fitting curves. The accuracy of the adsorption isotherm model was assessed via a comparison of the regression coefficient R^2 of two used models for all adsorbents. For all BC adsorbents, the Langmuir adsorption model was found to have a higher R^2 value than the Freundlich adsorption model through comparative analysis of the fitting curves. Therefore, the boron adsorption by the BC adsorbents is attributed to a single molecular layer at a uniform adsorption site, which means that the adsorption behavior of boric acid is influenced by a mechanism that is mediated by the surface properties of the adsorbent [55].

The adsorption kinetics of boron onto biochar (BC) adsorbents is illustrated through the qt vs. t1/2 plots, as depicted in Fig. 10 and Table 3. The findings indicate that the adsorption occurs in three distinct stages. Stage I involves the diffusion of boron to the external surfaces of the BC adsorbents, highlighting the influence of the boundary layer effect during the initial adsorption phase. Stage II corresponds to the intraparticle diffusion process, while Stage III represents the attainment of dynamic equilibrium [56].

3.6.6. Adsorption mechanism

Chemical and physical adsorption can occur for boron adsorption on BC adsorbents.

SEM analysis demonstrated that the BC adsorbents' surface contained an abundance of pores widely distributed throughout the surface, combined with a high surface area. This structure provided physical adsorption and pores diffusion of boron ions onto BC adsorbents [57]. Furthermore, the formation of complexes between boron ions and hydroxy functional groups influenced boron adsorption on the BC adsorbent's surface. This interaction between boron and adsorbent occurs due to the affinity of boron to form strong bonds with hydroxyl groups. The formation of boron complexes with hydroxyl groups of BC adsorbents relies on the boron species present in the solution, namely $[B(OH)_3]$ or $[B(OH)_4^-]$. The non-ionizing species predominantly exist in the $[B(OH)_3]$ form at pH = 7 or less. However, at pH values exceeding 9, the dominant boron species in boric acid solution shifts to $[B(OH)_4^-]$ [58]. The optimum pH for boron adsorption using various adsorbents in the present research was obtained at pH 8–9 for BC adsorbents. The primary boron species under these conditions was found to be $[B(OH)_4^-]$, indicating that the adsorption reaction primarily involves this species.

A simplified illustration is provided in Scheme 1.

3.6.7. Adsorption reusability

The reusability performance of the BC adsorbents was tested through 3 adsorption-desorption cycles. Fig. 11 indicated that the hydroxy-functionalized adsorbents' adsorption capacity decreased progressively with each cycle. This decrease can be due to the formation of stable complexes between diol groups and boron ions. Desorption was done in mild conditions (HCl, 0.1 M), and the adsorption sites of the BC adsorbents cannot be completely restored.

Using Table 4, this study compares the adsorption capacity of BC adsorbents against other boron adsorbents documented in the literature. Our findings indicate that the BC adsorbents prepared in this work have exhibited a significantly higher adsorption capacity when compared to other adsorbents examined, thereby demonstrating their potential application for boron removal.

4. Conclusion

In conclusion, hydroxy-functionalized biochar adsorbents were synthesized successfully for boron adsorption. The adsorbents were synthesized by straightforward experimental techniques from lignocellulosic biomass of date palm followed by different characterization methods. Using a batch adsorption method, various aspects of boron adsorption were investigated, including kinetics, isotherms, mechanism, and recycling. BC-PDA, MBC-PDA, BC-AlOOH, and BC-$ZnCl_2$ composites showed high adsorption capacity due to abundant -OH groups on their surfaces. The adsorption equilibrium values of BC, BC-PDA, MBC-PDA, BC-AlOOH, and BC-$ZnCl_2$ composites were achieved at 14, 20.5, 21.5, 43.2, and 44.2 mg/g, respectively, after 6 h. The ease of regeneration further enhanced the effectiveness of synthesized adsorbents. As a result, the developed adsorbents are effective and sustainable compounds for boron

Table 2
Langmuir and Freundlich equilibrium constants for boron adsorption by BC adsorbents.

model	Langmuir isotherm model			
Adsorbent	BC-PDA	MBC-PDA	BC-AlOOH	BC-$ZnCl_2$
q_{max}	24.10799	26.79056	52.69119	56.12503
k_L	0.4674	0.40872	0.43144	0.39527
R^2	0.9769	0.9837	0.98156	0.98596
model	Freundlich isotherm model			
1/n	10.23423	10.58566	21.42156	21.82396
k_F	0.21988	0.23757	0.23066	0.24119
R^2	0.76863	0.81321	0.79714	0.82044

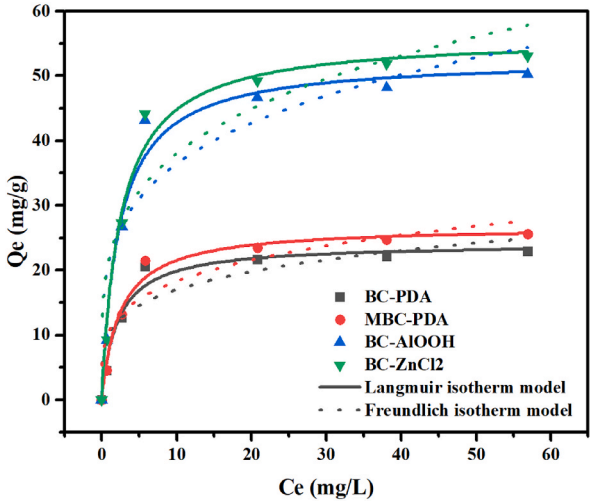

Fig. 9. Curves fitted with the Langmuir and Freundlich model for boron adsorption by BC adsorbents.

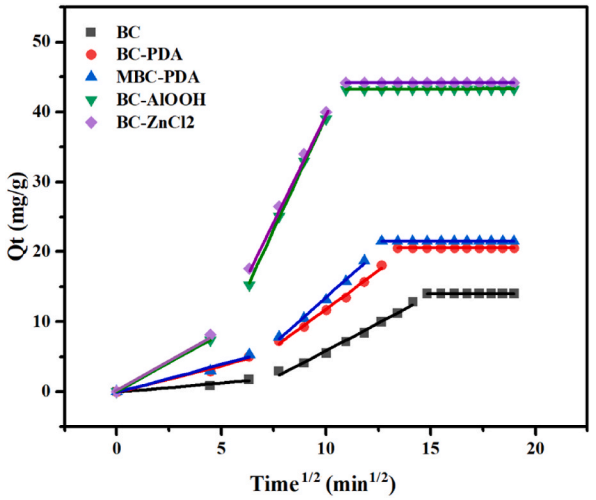

Fig. 10. Intraparticle diffusion model for boron adsorption by BC adsorbents.

Table 3
The parameters of intraparticle diffusion model for boron adsorption by BC adsorbents.

Adsorbent	Step I	Step II	Step III
	k_1 (mg/g min$^{1/2}$)	K_2 (mg/g min$^{1/2}$)	K_3 (mg/g min$^{1/2}$)
BC	0.2607	1.56078	0.00007
BC-PDA	0.76432	2.20166	0.00001
MBC-PDA	0.80713	2.64327	0.00001
BC-AlOOH	1.65469	6.49608	0.00001
BC-$ZnCl_2$	1.81122	6.1184	0.00001

removal in aqueous environments. The research highlights the potential of biochar-based adsorbents to address contemporary boron contamination challenges in the water treatment field.

CRediT authorship contribution statement

Sanaz Amirshekari: Methodology, Investigation, Formal analysis. **Saeid Shafiei:** Writing – review & editing, Writing – original draft, Visualization, Validation, Supervision, Software, Resources, Project administration, Methodology, Investigation, Funding

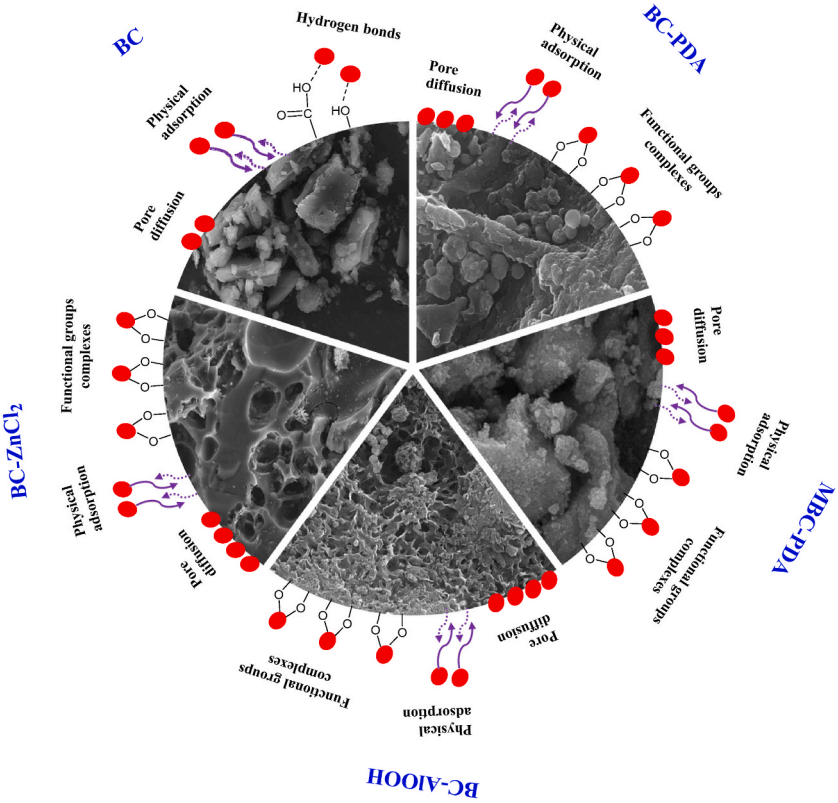

Scheme 1. Conceptual model of boron adsorption mechanism on adsorbents.

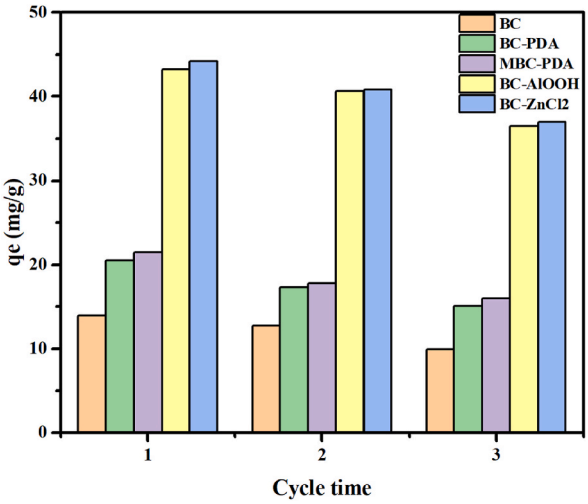

Fig. 11. Adsorption-desorption cycles of boron adsorption on BC adsorbents.

acquisition, Formal analysis, Data curation, Conceptualization. **Mahboobeh Zahedifar:** Writing – review & editing, Writing – original draft, Visualization, Validation, Supervision, Software, Resources, Project administration, Methodology, Investigation, Funding acquisition, Formal analysis, Data curation, Conceptualization. **Hossein Shekofteh:** Writing – review & editing, Writing – original draft, Conceptualization.

Table 4
Comparison of BC adsorbents efficiency with other reported carbon-based materials.

Adsorbent	C_0 (mg/L)	Q_e (mg/g)	t (min)	Ref
BC/ZIF-8	300	44	300	[52]
activated carbon from olive bagasse	100	3.5	3000	[54]
GO/ZIF-67	200	66.65	720	[59]
CVN	30	12.4	1200	[60]
BC-PDA	50	20.5	360	This work
MBC-PDA	50	21.5	360	This work
BC-AlOOH	50	43.2	360	This work
BC-$ZnCl_2$	50	44.2	360	This work

Data availability

Data will be made available on request.

Declaration of generative AI and AI-assisted technologies in the writing process

During the preparation of this work the author(s) used ChatGPT v3.5 in some parts to improve the language and flow of speech. After using this tool/service, the author(s) reviewed and edited the content as needed and take (s) full responsibility for the content of the publication.

Declaration of competing interest

The authors declare that they have no known competing financial interests or personal relationships that could have appeared to influence the work reported in this paper.

Acknowledgments

The authors express appreciation to the University of Jiroft Faculty Research Committee for supporting this investigation.

References

[1] T. Pan, X. Cui, Gelatin aerogel with good mechanical properties and adjustable physical properties for boron adsorption from salt lake brines: an optimized process, Int. J. Biol. Macromol. 251 (2023) 126403, https://doi.org/10.1016/j.ijbiomac.2023.126403.
[2] C. Minoia, C. Gregotti, A. Di Nucci, S.M. Candura, M. Tonini, L. Manzo, Toxicology and health impact of environmental exposure to boron. A review, G. Ital, Med. Lav. 9 (3–4) (1987) 119–124.
[3] E. Güler, C. Kaya, N. Kabay, M. Arda, Boron removal from seawater: state-of-the-art review, Desalination 356 (2015) 85–93, https://doi.org/10.1016/j.desal.2014.10.009.
[4] Ü. Gemici, G. Tarcan, Distribution of boron in thermal waters of western Anatolia, Turkey, and examples of their environmental impacts, Environ. Geol. 43 (1) (2002) 87–98, https://doi.org/10.1007/s00254-002-0608-x.
[5] K. Yıldırım, G.Ç. Kasım, Phytoremediation potential of poplar and willow species in small scale constructed wetland for boron removal, Chemosphere 194 (2018) 722–736, https://doi.org/10.1016/j.chemosphere.2017.12.036.
[6] B. Ozbey-Unal, D.Y. Imer, B. Keskinler, I. Koyuncu, Boron removal from geothermal water by air gap membrane distillation, Desalination 433 (2018) 141–150, https://doi.org/10.1016/j.desal.2018.01.033.
[7] N.B. Darwish, A. Alkhudhiri, A. AlAlawi, H. AlRomaih, N. Hilal, Experimental investigation of forward osmosis process for boron removal from water, J. Water Process Eng. 38 (2020) 101570, https://doi.org/10.1016/j.jwpe.2020.101570.
[8] A. Alkhudhiri, N. Bin Darwish, M.W. Hakami, A. Abdullah, A. Alsadun, H. Abu Homod, Boron removal by membrane distillation: a comparison study, Membranes 10 (2020) 263, https://doi.org/10.3390/membranes10100263.
[9] G. Sayiner, F. Kandemirli, A. Dimoglo, Evaluation of boron removal by electrocoagulation using iron and aluminum electrodes, Desalination 230 (1) (2008) 205–212, https://doi.org/10.1016/j.desal.2007.10.020.
[10] C. Irawan, Y.-L. Kuo, J.C. Liu, Treatment of boron-containing optoelectronic wastewater by precipitation process, Desalination 280 (1) (2011) 146–151, https://doi.org/10.1016/j.desal.2011.06.064.
[11] A. Hussain, R. Sharma, J. Minier-Matar, Z. Hirani, S. Adham, Application of emerging ion exchange resin for boron removal from saline groundwater, J. Water Process Eng. 32 (2019) 100906, https://doi.org/10.1016/j.jwpe.2019.100906.
[12] E. Babiker, M.A. Al-Ghouti, N. Zouari, G. McKay, Removal of boron from water using adsorbents derived from waste tire rubber, J. Environ. Chem. Eng. 7 (2) (2019) 102948, https://doi.org/10.1016/j.jece.2019.102948.
[13] J. Kluczka, W. Pudło, K. Krukiewicz, Boron adsorption removal by commercial and modified activated carbons, Chem. Eng. Res. Des. 147 (2019) 30–42, https://doi.org/10.1016/j.cherd.2019.04.021.
[14] S.A. Valverde, J.C.V. Azevedo, A.B. França, I.J.B. Santos, F.L. Naves, P.L. Mesquita, Removal of boron from water by batch adsorption onto bovine bone char: optimization, kinetics and equilibrium, Int. J. Environ. Sci. Technol. 20 (2023) 9423–9440, https://doi.org/10.1007/s13762-022-04643-5.
[15] B. Wang, H. Lin, X. Guo, P. Bai, Boron removal using chelating resins with pyrocatechol functional groups, Desalination 347 (2014) 138–143, https://doi.org/10.1016/j.desal.2014.05.035.
[16] A. Iizuka, M. Takahashi, T. Nakamura, A. Yamasaki, Boron removal performance of a solid sorbent derived from waste concrete, Ind. Eng. Chem. Res. 53 (10) (2014) 4046–4051, https://doi.org/10.1021/ie402176t.
[17] T. Vermeulen, Separation by adsorption methods, in: T.B. Drew, J.W. Hoopes (Eds.), Advances in Chemical Engineering, Academic Press1958, pp. 147-208.
[18] A. Nematollahzadeh, Z. Vaseghi, Biosorbents in industrial wastewater treatment, in: T. Karchiyappan, R.R. Karri, M.H. Dehghani (Eds.), Industrial Wastewater Treatment : Emerging Technologies for Sustainability, Springer International Publishing, Cham, 2022, pp. 101–132.
[19] A. Srivastava, P.K. Mathur, V.P. Sharma, Chapter 19 - studies of wastewater treatment techniques using low-cost biosorbents, in: M. Shah, S. Rodriguez-Couto (Eds.), Microbial Ecology of Wastewater Treatment Plants, Elsevier2021, pp. 395-410.

[20] A. Fdez-Sanromán, M. Pazos, E. Rosales, M.A. Sanromán, Unravelling the environmental application of biochar as low-cost biosorbent: a review, Appl. Sci. 10 (2020) 7810–7832, https://doi.org/10.3390/app10217810.

[21] M. Zahedifar, N. Seyedi, M. Salajeghe, S. Shafiei, Nanomagnetic biochar dots coated silver NPs (BCDs-Ag/MNPs): a highly efficient catalyst for reduction of organic dyes, Mater. Chem. Phys. 246 (2020) 122789, https://doi.org/10.1016/j.matchemphys.2020.122789.

[22] M. Ahmad, A.U. Rajapaksha, J.E. Lim, M. Zhang, N. Bolan, D. Mohan, M. Vithanage, S.S. Lee, Y.S. Ok, Biochar as a sorbent for contaminant management in soil and water: a review, Chemosphere 99 (2014) 19–33, https://doi.org/10.1016/j.chemosphere.2013.10.071.

[23] S.Y. Foong, K.Y. Cheong, S.H. Kong, C.L. Yiin, P.N.Y. Yek, R. Safdar, R.K. Liew, S.K. Loh, S.S. Lam, Recent progress in the production and application of biochar and its composite in environmental biodegradation, Bioresour. Technol. 387 (2023) 129592, https://doi.org/10.1016/j.biortech.2023.129592.

[24] D. Mohan, A. Sarswat, Y.S. Ok, C.U. Pittman, Organic and inorganic contaminants removal from water with biochar, a renewable, low cost and sustainable adsorbent – a critical review, Bioresour. Technol. 160 (2014) 191–202, https://doi.org/10.1016/j.biortech.2014.01.120.

[25] X. Gai, H. Wang, J. Liu, L. Zhai, S. Liu, T. Ren, H. Liu, Effects of feedstock and pyrolysis temperature on biochar adsorption of ammonium and nitrate, PLoS One 9 (12) (2014) e113888, https://doi.org/10.1371/journal.pone.0113888.

[26] J. Wang, P. Zhang, J. Peng, Q. Zhang, J. Yao, X. Wu, Y. Li, Sulfur and nitrogen co-doped magnetic biochar coupled with hydroxylamine for high-efficiency of persulfate activation and mechanism study, Environ. Res. 216 (2023) 114745, https://doi.org/10.1016/j.envres.2022.114745.

[27] Y. Antit, I. Olivares, M. Hamdi, S. Sánchez, Biochemical conversion of lignocellulosic biomass from date palm of Phoenix dactylifera L. Into ethanol production, Energies 14 (2021) 1887, https://doi.org/10.3390/en14071887.

[28] W.-H. Huang, Y.-J. Chang, D.-J. Lee, Layered double hydroxide loaded pinecone biochar as adsorbent for heavy metals and phosphate ion removal from water, Bioresour. Technol. 391 (2024) 129984, https://doi.org/10.1016/j.biortech.2023.129984.

[29] S. Wan, S. Wang, Y. Li, B. Gao, Functionalizing biochar with Mg–Al and Mg–Fe layered double hydroxides for removal of phosphate from aqueous solutions, J. Ind. Eng. Chem. 47 (2017) 246–253, https://doi.org/10.1016/j.jiec.2016.11.039.

[30] C. Zhao, J. Ma, Z. Li, H. Xia, H. Liu, Y. Yang, Highly enhanced adsorption performance of tetracycline antibiotics on KOH-activated biochar derived from reed plants, RSC Adv. 10 (9) (2020) 5066–5076, https://doi.org/10.1039/C9RA09208K.

[31] M. Zahedifar, N. Seyedi, Bare 3D-TiO2/magnetic biochar dots (3D-TiO2/BCDs MNPs): highly efficient recyclable photocatalyst for diazinon degradation under sunlight irradiation, Phys. E: Low-Dimens. Syst. Nanostructures. (2022) 115151, https://doi.org/10.1016/j.physe.2022.115151.

[32] M. Zahedifar, N. Seyedi, R. Razavi, In situ fabrication of Ag2S/Ag2SO4 on the chitosan NP matrix for enhanced photodegradation of rhodamine B dye contaminant under visible light, Biomass Conv. Bioref. 14 (2022) 10011–10026, https://doi.org/10.1007/s13399-022-03094-9.

[33] S. Shi, J. Yang, S. Liang, M. Li, Q. Gan, K. Xiao, J. Hu, Enhanced Cr(VI) removal from acidic solutions using biochar modified by Fe3O4@SiO2-NH2 particles, Sci. Total Environ. 628–629 (2018) 499–508, https://doi.org/10.1016/j.scitotenv.2018.02.091.

[34] H. Li, D. Jiang, Z. Huang, K. He, G. Zeng, A. Chen, L. Yuan, M. Peng, T. Huang, G. Chen, Preparation of silver-nanoparticle-loaded magnetic biochar/poly (dopamine) composite as catalyst for reduction of organic dyes, J. Colloid Interface Sci. 555 (2019) 460–469, https://doi.org/10.1016/j.jcis.2019.08.013.

[35] M. Zahedifar, P. Mohammadi, H. Sheibani, Synthesis and characterization of novel magnetic nanoparticles supported imidazole ion as an efficient catalytic system for the three-component reaction of arylaldehydes, malononitrile and α-hydroxy or α-amino active methylene compounds, Lett. Org. Chem. 14 (5) (2017) 315–323, https://doi.org/10.2174/1570178614666170329152804.

[36] M. Zhang, B. Gao, Removal of arsenic, methylene blue, and phosphate by biochar/AlOOH nanocomposite, Chem. Eng. J. 226 (2013) 286–292, https://doi.org/10.1016/j.cej.2013.04.077.

[37] D. Xia, F. Tan, C. Zhang, X. Jiang, Z. Chen, H. Li, Y. Zheng, Q. Li, Y. Wang, ZnCl2-activated biochar from biogas residue facilitates aqueous As(III) removal, Appl. Surf. Sci. 377 (2016) 361–369, https://doi.org/10.1016/j.apsusc.2016.03.109.

[38] R. Keren, Boron, Methods of Soil Analysis1996, pp. 603-626.

[39] Y. Gao, A. Pramanik, S. Begum, C. Sweet, S. Jones, A. Alamgir, P.C. Ray, Multifunctional biochar for highly efficient capture, identification, and removal of toxic metals and superbugs from water samples, ACS Omega 2 (11) (2017) 7730–7738, https://doi.org/10.1021/acsomega.7b01386.

[40] J. Zhao, M. Ma, X. Yan, G. Zhang, J. Xia, Z. Zeng, P. Yu, Q. Deng, D. Gong, Green synthesis of polydopamine functionalized magnetic mesoporous biochar for lipase immobilization and its application in interesterification for novel structured lipids production, Food Chem. 379 (2022) 132148, https://doi.org/10.1016/j.foodchem.2022.132148.

[41] Q. Yin, H. Ren, R. Wang, Z. Zhao, Evaluation of nitrate and phosphate adsorption on Al-modified biochar: influence of Al content, Sci. Total Environ. 631–632 (2018) 895–903, https://doi.org/10.1016/j.scitotenv.2018.03.091.

[42] R.L. Frost, J.T. Kloprogge, Infrared emission spectroscopic study of brucite, Spectrochim. Acta Mol. Biomol. Spectrosc. 55 (11) (1999) 2195–2205, https://doi.org/10.1016/S1386-1425(99)00016-5.

[43] T. Wen, J. Wang, S. Yu, Z. Chen, T. Hayat, X. Wang, Magnetic porous carbonaceous material produced from tea waste for efficient removal of as(V), Cr(VI), humic acid, and dyes, ACS Sustain. Chem. Eng. 5 (5) (2017) 4371–4380, https://doi.org/10.1021/acssuschemeng.7b00418.

[44] R. Shojaei, M. Zahedifar, P. Mohammadi, K. Saidi, H. Sheibani, Novel magnetic nanoparticle supported ionic liquid as an efficient catalyst for the synthesis of spiro [pyrazole-pyrazolo[3,4-b]pyridine]-dione derivatives under solvent free conditions, J. Mol. Struct. 1178 (2019) 401–407, https://doi.org/10.1016/j.molstruc.2018.10.052.

[45] M. Zahedifar, B. Pouramiri, R. Razavi, Triethanolamine lactate-supported nanomagnetic cellulose: a green and efficient catalyst for the synthesis of pyrazolo [3,4-b]quinolines and theoretical study, Res. Chem. Intermed. 46 (5) (2020) 2749–2765, https://doi.org/10.1007/s11164-020-04117-8.

[46] K.-W. Jung, B.H. Choi, T.-U. Jeong, K.-H. Ahn, Facile synthesis of magnetic biochar/Fe3O4 nanocomposites using electro-magnetization technique and its application on the removal of acid orange 7 from aqueous media, Bioresour. Technol. 220 (2016) 672–676, https://doi.org/10.1016/j.biortech.2016.09.035.

[47] R. Han, W. Li, W. Pan, M. Zhu, D. Zhou, F.-s. Li, 1D magnetic materials of Fe3O4 and Fe with high performance of microwave absorption fabricated by electrospinning method, Sci. Rep. 4 (1) (2014) 7493, https://doi.org/10.1038/srep07493.

[48] A. Abbasi, W.Z.N. Yahya, M.M. Nasef, M. Moniruzzaman, A.S.M. Ghumman, H.K. Afolabi, Boron removal by glucamine-functionalized inverse vulcanized sulfur polymer, React. Funct. Polym. 177 (2022) 105311, https://doi.org/10.1016/j.reactfunctpolym.2022.105311.

[49] Y. Inukai, Y. Tanaka, T. Matsuda, N. Mihara, K. Yamada, N. Nambu, O. Itoh, T. Doi, Y. Kaida, S. Yasuda, Removal of boron(III) by N-methylglucamine-type cellulose derivatives with higher adsorption rate, Anal. Chim. Acta 511 (2) (2004) 261–265, https://doi.org/10.1016/j.aca.2004.01.054.

[50] A.A. Oladipo, M. Gazi, Hydroxyl-enhanced magnetic chitosan microbeads for boron adsorption: parameter optimization and selectivity in saline water, React. Funct. Polym. 109 (2016) 23–32, https://doi.org/10.1016/j.reactfunctpolym.2016.09.005.

[51] C. Sanfeliu, R. Martínez-Máñez, F. Sancenón, J. Soto, V. Puchol, P. Amorós, M.D. Marcos, Low-cost materials for boron adsorption from water, J. Mater. Chem. 22 (48) (2012) 25362–25372, https://doi.org/10.1039/C2JM32819D.

[52] M. Luo, C. Zhu, Q. Chen, F. Song, W. Hao, Z. Shen, K.O. Konhauser, D.S. Alessi, C. Zhong, In-situ growth of ZIF-8 nanocrystals on biochar for boron adsorption, Colloids Surf. A: Physicochem. Eng. Asp. 657 (2023) 130504, https://doi.org/10.1016/j.colsurfa.2022.130504.

[53] T. Taghipour, G. Karimipour, M. Ghaedi, A. Asfaram, Mild synthesis of a Zn(II) metal organic polymer and its hybrid with activated carbon: application as antibacterial agent and in water treatment by using sonochemistry: optimization, kinetic and isotherm study, Ultrason. Sonochem. 41 (2018) 389–396, https://doi.org/10.1016/j.ultsonch.2017.09.056.

[54] T.E. Köse, H. Demiral, N. Öztürk, Adsorption of boron from aqueous solutions using activated carbon prepared from olive bagasse, Desalin. Water Treat. 29 (1–3) (2011) 110–118, https://doi.org/10.5004/dwt.2011.2091.

[55] W. Wang, H. Li, Y. Zhou, J. Pan, Investigation of the mechanism of establishing a solid–water–oil system by metastable droplets and their application in the fabrication of polyol nanosheets for rapid boron removal, Chem. Eng. J. 475 (2023) 145930, https://doi.org/10.1016/j.cej.2023.145930.

[56] M. Zhang, K. Zhang, J. Wang, R. Zhou, J. Li, W. Zhao, Study on optimal adsorption conditions of norfloxacin in water based on response surface methodology, Water Supply 22 (4) (2022) 3661–3672, https://doi.org/10.2166/ws.2022.008.

[57] M. Zahedifar, N. Seyedi, S. Shafiei, M. Basij, Surface-modified magnetic biochar: highly efficient adsorbents for removal of Pb(II) and Cd(II), Mater. Chem. Phys. 271 (2021) 124860, https://doi.org/10.1016/j.matchemphys.2021.124860.

[58] Y.Y. Le, Y. Guan, X. Ma, W. Zhang, Preparation and boron removal performance of glycidol modified PANI nanorods: an optimization study based on response surface methodology, Polymers 15 (2023) 459, https://doi.org/10.3390/polym15020459.
[59] G. Hu, W. Zhang, Y. Chen, C. Xu, R. Liu, Z. Han, Removal of boron from water by GO/ZIF-67 hybrid material adsorption, Environ. Sci. Pollut. Res. 27 (22) (2020) 28396–28407, https://doi.org/10.1007/s11356-020-08018-6.
[60] S. Liu, M. Xu, T. Yu, D. Han, J. Peng, J. Li, M. Zhai, Radiation synthesis and performance of novel cellulose-based microsphere adsorbents for efficient removal of boron (III), Carbohydr. Polym. 174 (2017) 273–281, https://doi.org/10.1016/j.carbpol.2017.06.012.